



## Article

# Assessing Height Variations in Qinghai-Tibet Plateau from Time-Varying Gravity Data and Hydrological Model

Tong Shi <sup>1</sup>, Jinyun Guo <sup>1,\*</sup> , Haoming Yan <sup>2</sup>, Xiaotao Chang <sup>3</sup>, Bing Ji <sup>4</sup> and Xin Liu <sup>1</sup><sup>1</sup> College of Geodesy and Geomatics, Shandong University of Science and Technology, Qingdao 266590, China<sup>2</sup> State Key Laboratory of Geodesy and Earth's Dynamics, Innovation Academy for Precision Measurement Science and Technology, Chinese Academy of Sciences, Wuhan 430077, China<sup>3</sup> Land Satellite Remote Sensing Application Center, Ministry of Natural Resources, Beijing 100048, China<sup>4</sup> Department of Navigation Engineering, Naval University of Engineering, Wuhan 430033, China

\* Correspondence: guojy@sdust.edu.cn

**Abstract:** Height variations caused by mass change make an important contribution to the tectonic uplift of the Qinghai-Tibet Plateau (QTP). To study the deformation attributable to hydrological loading and real potential tectonic vertical motion, satellite gravity data from the Gravity Recovery and Climate Experiment (GRACE) and GRACE Follow-On (GRACE-FO) with data from the Global Land Data Assimilation System (GLDAS) and Global Positioning System (GPS) are adopted to estimate height variations in QTP. Based on spherical harmonic function (SHF) and Green's function (GF), the results show the trend of height variations is unevenly distributed in the spatial domain. The SHF indicated that the rate in the southwest of the QTP is ~1 mm/year, while the northern and eastern show a subtle decreasing trend, which indicates hydrological loading is not the main cause of the uplift observed with GRACE. The maximum annual amplitude of height variations is ~12 mm, reaching the annual maximum around February to March. The average correlation coefficients of SHF, and GF height variations with GPS heights are 0.70 and 0.82, respectively. Based on cross wavelet transform, it is concluded that there are annual signals between the height variations derived from GPS with GRACE (-FO) and GLDAS. Finally, the tectonic vertical motion in the QTP is given by removing the effect of hydrological loading, which shows most GPS stations are uplifted at a rate of 0.06 mm/year–1.97 mm/year.

**Keywords:** GRACE; GLDAS; height variations; Qinghai-Tibet Plateau

**Citation:** Shi, T.; Guo, J.; Yan, H.; Chang, X.; Ji, B.; Liu, X. Assessing Height Variations in Qinghai-Tibet Plateau from Time-Varying Gravity Data and Hydrological Model. *Remote Sens.* **2022**, *14*, 4707. <https://doi.org/10.3390/rs14194707>

Academic Editor: Chung-yen Kuo

Received: 20 August 2022

Accepted: 19 September 2022

Published: 21 September 2022

**Publisher's Note:** MDPI stays neutral with regard to jurisdictional claims in published maps and institutional affiliations.



**Copyright:** © 2022 by the authors. Licensee MDPI, Basel, Switzerland. This article is an open access article distributed under the terms and conditions of the Creative Commons Attribution (CC BY) license (<https://creativecommons.org/licenses/by/4.0/>).

## 1. Introduction

The Qinghai-Tibet Plateau (QTP, 25°N–40°N, 74°E–104°E) with an average altitude of more than 4000 m, known as the third pole, is a tectonic extrusion and deformation zone as result of the collision between the Indian and Eurasian plates [1]. Accurate determination of height variations over the QTP is important for the study of plate movement and evolution, and ecological changes [2]. The continuous uplift and geophysical processes of the QTP have always been a controversial issue [3]. The traditional method of obtaining height variations mainly relies on precise levelling measurements [4]. With the development of space geodesy technology, GPS network provides high-precision quantitative data of crustal motion by observing the coordinate changes of GPS stations [5–7]. The GPS vertical coordinates mainly include linear trends and seasonal variations at annual scales, while the causes of linear trends include tectonic and non-tectonic motions (e.g., mass change) and other factors [6]. Liang et al. [8] estimated the three-dimensional velocity field for the QTP, with the Himalayan Mountains uplifting of 2 mm/year. Moreover, repeated absolute gravity measurements are also sensitive to mass migration and vertical deformation of the surface. Xing et al. [9] combined high-precision absolute gravity measurements and GPS data to quantify the average uplift rate of 1.4 mm/year on the QTP. Van Camp et al. [10] discussed the tectonic interpretation from stations in Tibet using absolute gravity survey.

Bayesian gravity adjustment could also apply for the hybrid gravity survey network to estimate crustal mass redistributions in QTP [11].

GRACE was launched in March 2002, and its main mission is to detect time-varying gravity because of Earth's mass distribution [12,13], which has been generally used for global or regional terrestrial water storage (TWS) changes [14–21], dynamic monitoring of glacier and polar masses [22], etc. GRACE-FO was launched in May 2018 to take over the scientific mission of GRACE. Goncalves et al. [17] argued that a basin scale water budget involving GRACE solutions is an operative and efficient way to estimate the region-wide recharge of a large confined-unconfined aquifer system. GRACE-derived TWS is the composition of various water storage components, i.e., soil moisture storage, snow and surface water storage, and groundwater storage [13]. Recent research has demonstrated that GRACE combined with hydrological data can detect variations in the composition of TWS in large areas over the last two decades [18–20,23]. Othman et al. [13] showed a reliable calculation of the water budget in Iraq using GRACE-derived TWS and groundwater. Abhishek et al. [19] quantified the GRACE-derived TWS and groundwater to investigate major flood and drought event of the Chao Phraya River Basin, which will efficiently sustain the basin's socio-economic activities.

According to the theory of elastic loading [24], the GRACE time-varying gravity field model not only allows the gravitational field detect changes in hydrological mass, but also estimate the vertical deformation on the surface due to the corresponding changes. Duan et al. [25] obtained the uplift rate of QTP using GRACE gravity data by removing the gravity effect of TWS. In addition, the surface loading model could reveal the variations of surface loading caused by atmospheric, hydrological, and non-tidal oceanic factors [26]; van Dam and Wahr [27] argued that the vertical displacement due to atmospheric loading is 15–20 mm obtained by Green's function.

Tectonic motion and seasonal surface deformations in the QTP can be determined by time-variable satellite gravity data, GPS, and surface loading model with continually increasing data density and precision. Zou et al. [28] found that the summer monsoon and precipitation cause seasonal variations in southern Tibet. Sun et al. [2] confirmed that the thickness of the earth's crust is increasing at a rate of millimeters to decimeters per year of the QTP from gravity data and GPS measurements. Liu et al. [29] derived the crustal thickening rate of 3 mm/year by GRACE data over the QTP. The highest uplift rate of the QTP is location in Longmen Shan fault, at a rate of ~7–9 mm/year [26,30]. Groundwater is not significant in the signals of QTP derived from GRACE, and mainly caused by tectonic movements [31]. In general, it has been confirmed that the QTP continues to uplift, both strong seasonal fluctuations and long-term trends are observed. However, there are some issues when evaluating tectonic motion and seasonal surface deformations in QTP, e.g., different data processing methods, less data used, not removed hydrological signals, and short research period.

Thus, this study estimates the height variations caused by the hydrological mass change in the QTP based on comprehensive comparisons the geodetic and hydrological model. This paper is organized as follows. In Section 2, the study data, e.g., GRACE time-varying gravity field model, GLDAS hydrological model and GPS data are briefly explained. In Section 3, the methods of estimating height variations are presented. In Section 4, long-term trend and annual signals of height variations in QTP are analyzed and the correlation of results derived from different datasets is assessed. In Section 5, the tectonic motion is presented where the effect of the hydrological loading is eliminated in GPS vertical deformation.

## 2. Study Data

### 2.1. Time-Varying Gravity Data

The GRACE (-FO) RL06 Level-2 data released by the Center for Space Research (CSR, <https://www2.csr.utexas.edu/grace/RL06.html>, accessed on 1 December 2021) [32] are used to estimate the height variations from April 2002 to December 2020. Linear



The raw GPS observations are processed by the GAMIT/GLOBK software [39] with the orbit and clock bias provided by International GNSS Service (IGS). The tropospheric delays are corrected using the Global Mapping Function (GMF) model and the ionospheric effects are weakened based on the ionosphere-free combinations. The antenna phase center is corrected by the IGS antenna model, the solid tide, and the polar tide is corrected using the International Earth Rotation Service 2003 (IERS03) model, and the ocean tide loading effects are corrected by the Finite Element Solution 2004 (FES2004) model. The GNSS Missing Data Interpolation Software (GMIS) [40] is used to fill in the missing GPS data.

The signal of environmental loading in the GPS vertical coordinate mainly includes non-tidal atmospheric loading (NTAL), non-tidal ocean loading (NTOL), and hydrological loading. Since the surface vertical deformation derived from GRACE (-FO) gravity solutions mainly contains hydrological loading, NTAL and NTOL in the GPS need to be removed. The Modern-Era Retrospective analysis for Research and Applications, Version 2 (MERRA2) [41] atmospheric loading model, and the Max Planck Institute Ocean Model (MPIOM06) [42] non-tidal ocean loading model provided by the International Mass Load Service (<http://massloading.net/>, accessed on 7 November 2021) [43] are taken to process GPS vertical coordinate in this paper. The annual amplitudes of NTAL and NTOL at the GPS stations are shown in Figure 2. Compared with the NTOL, NTAL has a greater impact on the QTP, with the maximum annual amplitude up to 4.1 mm. The amplitude of NTAL is inversely proportional to the altitude, and the edge of the study area is more affected by NTAL than the internal high-altitude region. The maximum annual amplitude of the NTOL is about 0.4 mm, with an east-west distribution, i.e., high in the west and low in the east.

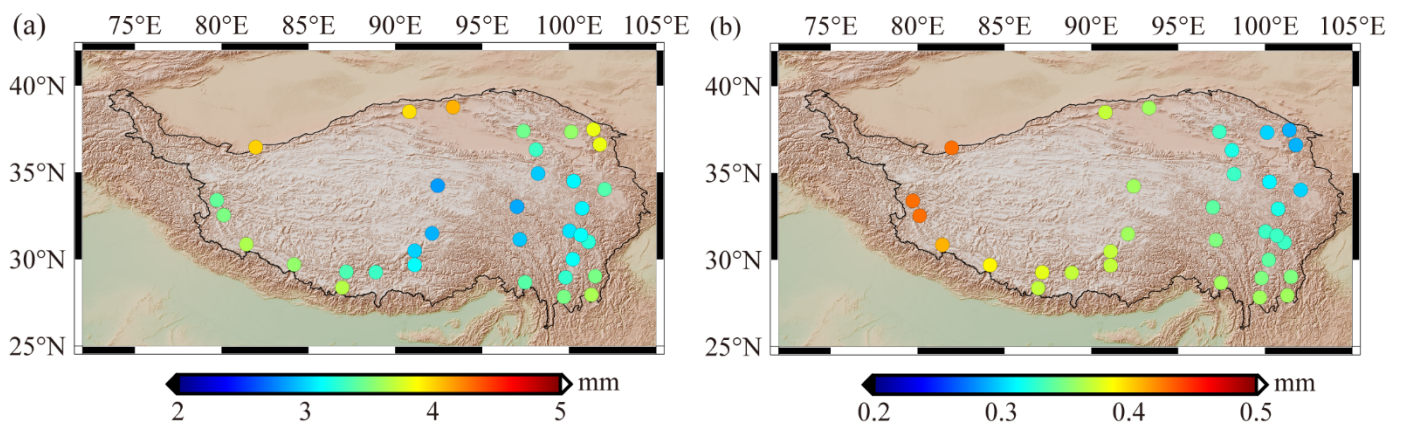


**Figure 2.** Annual vertical displacement amplitude of (a) non-tidal atmospheric loading (NTAL) and (b) non-tidal oceanic loading (NTOL) at GPS stations. The background color represents topography.

In addition, the contribution of the thermoelastic effect to the GPS bedrock is at the millimeter level on the global scale [44]. The bedrock thermal expansion [45] of 34 GPS stations is estimated using 1 km monthly temperature data [46] in this paper. Figure 3 shows the annual amplitude of bedrock thermal expansion, which increases from 0.76 mm to 1.49 mm with increasing latitude. The bedrock thermal expansion is deducted from the GPS vertical displacement to eliminate the effect of temperature change.

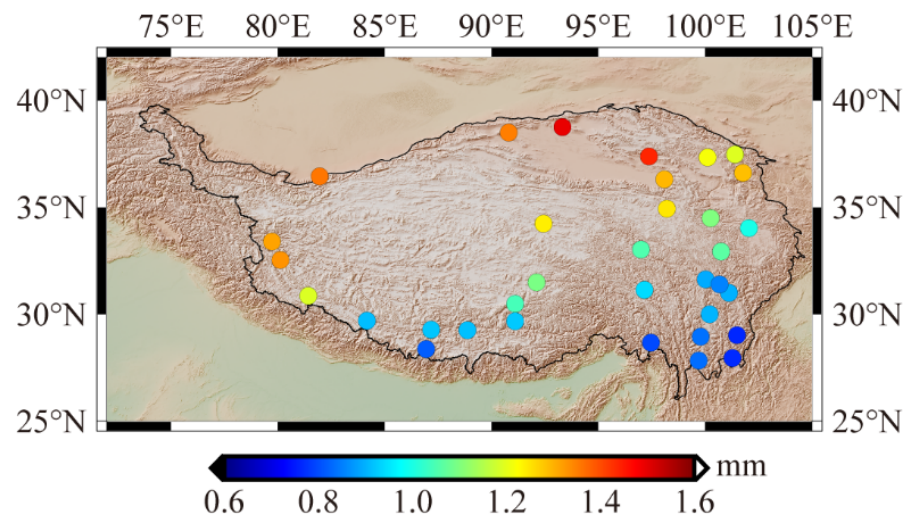


**Figure 3.** Annual vertical displacement amplitude of bedrock thermal expansion at GPS stations. The background color represents topography.

### 3. Research Methodology

#### 3.1. Height Variations

Height variations  $\Delta H$  represent the change in orthometric height (above the geoid) in this paper, which are determined as follows:

$$\Delta H = \Delta h - \Delta N \quad (1)$$

where  $\Delta N$  and  $\Delta h$  represent the temporal variation of geoid height and surface vertical displacement, respectively.

The gravity field is usually represented in the form of the geoid. Temporal variation of geoid height  $\Delta N$  can be estimated by the spherical harmonic function [47]:

$$\Delta N_{(r,\varphi,\lambda)} = \frac{GM}{r\gamma} \sum_{l=0}^{l_{\max}} \left(\frac{a}{r}\right)^l \sum_{m=0}^l (\Delta\bar{C}_{lm} \cos m\lambda + \Delta\bar{S}_{lm} \sin m\lambda) \bar{P}_{lm}(\sin \varphi) \quad (2)$$

where  $(r, \varphi, \lambda)$  are geocentric radius, latitude, and longitude on the ellipsoid, respectively,  $GM$  is the constant of earth gravitation,  $a$  is the semi-major axis of the reference ellipsoid,  $l$  and  $m$  are the degree and order of the spherical harmonic coefficients, respectively,  $l_{\max}(= 60)$  is the maximum degree of the spherical harmonic coefficient,  $\bar{P}_{lm}$  are the fully normalized Legendre functions of degree  $l$  and order  $m$ ,  $\gamma$  represents the normal gravity at the computation point,  $\Delta\bar{C}_{lm}$  and  $\Delta\bar{S}_{lm}$  derived from GRACE (-FO) is the residual of fully normalized Stokes coefficients, from which the average Stokes coefficients over the study period have been subtracted.

The surface vertical displacement  $\Delta h$  is determined by two methods in this paper, the spherical harmonic function (SHF), and Green's function (GF), which are described in Sections 3.1.1 and 3.1.2, respectively.

##### 3.1.1. Spherical Harmonic Function

The height variations  $\Delta H^{\text{SHF}}$  are estimated by the GRACE (-FO) time-varying gravity field model. Based on the earth loading deformation and gravity field theory [48], the surface vertical displacement is determined by the spherical harmonic coefficient derived from GRACE (-FO) as follows:

$$\Delta h^{\text{SHF}} = \frac{3a\rho_w}{\rho_{\text{ave}}} \sum_{l=0}^{l_{\max}} \sum_{m=0}^l (\Delta\bar{C}_{lm}^{\sigma} \cos m\lambda + \Delta\bar{S}_{lm}^{\sigma} \sin m\lambda) \frac{h_l}{2l+1} \bar{P}_{lm}(\sin \varphi) \quad (3)$$

where  $\Delta h^{\text{SHF}}$  is the geometric height change (above the ellipsoid) assuming that the gravity changes measured by GRACE are the result of changes in mass loading,  $\rho_w$  is the water density,  $\rho_{\text{ave}}$  is the earth's average density,  $h_l$  is the load Love numbers of degree  $l$ , and surface density Stokes coefficient  $\Delta \bar{C}_{lm}^\sigma$  and  $\Delta \bar{S}_{lm}^\sigma$  defined as:

$$\begin{cases} \Delta \bar{C}_{lm}^\sigma \\ \Delta \bar{S}_{lm}^\sigma \end{cases} = \frac{\rho_{\text{ave}}}{3\rho_w} \frac{2l+1}{1+k_l} \begin{cases} \Delta \bar{C}_{lm} \\ \Delta \bar{S}_{lm} \end{cases} \quad (4)$$

Combining Equations (3) and (4) obtains the vertical deformation due to mass change by the time-varying GRACE (-FO) gravity model:

$$\Delta h^{\text{SHF}} = a \sum_{l=0}^{l_{\text{max}}} \sum_{m=0}^l (\Delta \bar{C}_{lm} \cos m\lambda + \Delta \bar{S}_{lm} \sin m\lambda) \frac{h_l}{k_l+1} \bar{P}_{lm}(\sin \varphi) \quad (5)$$

where the load Love numbers  $h_l$  and  $k_l$  based on the Preliminary Reference Earth Model (PREM) [49] obtained from Wang et al. [50].

### 3.1.2. Green's Function

The height variations  $\Delta h^{\text{GF}}$  are determined by Green's function (GF) according to the elastic half-space model [24]. The  $\Delta h^{\text{GF}}$  can be determined as follows [51], which is a simplification of the usual load theory based on Farrell [24]:

$$\Delta h^{\text{GF}} = -2\rho_w \cdot \Delta EWT \cdot R_0 \cdot g \frac{1-\nu^2}{E} \quad (6)$$

where  $\Delta EWT$  is the time-variation of equivalent water thickness derived from the GLDAS hydrologic model,  $R_0$  is estimated by assuming a disk loading corresponding to the radius based on the spatial resolution of GRACE satellite missions' data ( $R_0 = \text{ca. } 167 \text{ km}$ ),  $g$  is the gravitational acceleration,  $\nu$  is the Poisson's ratio, and  $E$  is Young's modulus. The Poisson's ratio  $\nu$  is generally set to 0.25 [52]. The type of rock in the QTP is mainly syenite-diopside and granite-biotite; therefore, the  $E$  value is estimated to be 50 GPa in this study.

### 3.2. Least Square Fitting

The least squares spectral analysis is used to estimate the long-term trend, annual and semi-annual signals of height variations, which is as follows [53]:

$$y(t_i) = a + bt_i + c \sin(2\pi t_i) + d \cos(2\pi t_i) + e \sin(4\pi t_i) + f \cos(4\pi t_i) + v_i \quad (7)$$

where  $t_i$  is the epoch in unit of year,  $a$  and  $b$  are constant term and linear long-term trend, respectively, the coefficients  $(c, d)$  and  $(e, f)$  describe the annual and semi-annual amplitudes, respectively,  $v_i$  is the residual.

Time series of annual and semi-annual amplitudes ( $A_{\text{ann}}$  and  $A_{\text{semi-ann}}$ ) and phase ( $\varphi_{\text{ann}}$  and  $\varphi_{\text{semi-ann}}$ ) can be expressed as:

$$\begin{cases} A_{\text{ann}} = \sqrt{c^2 + d^2} \\ A_{\text{semi-ann}} = \sqrt{e^2 + f^2} \end{cases} \quad (8)$$

$$\begin{cases} \varphi_{\text{ann}} = \arctan(d/c) \\ \varphi_{\text{semi-ann}} = \arctan(f/e) \end{cases} \quad (9)$$

## 4. Results and Analysis

### 4.1. Height Variations on the QTP

According to the GRACE (-FO) temporal gravity field model, the geoid changes  $\Delta N$  are obtained by Equation (2), and the vertical surface deformation  $\Delta h$  estimated by SHF, and GF methods are derived by Equations (5) and (6), respectively. The height variation

$\Delta H$  is determined by the  $\Delta N$  and the  $\Delta h$  through Equation (1). The time series of  $\Delta N$ ,  $\Delta h$ , and  $\Delta H$  are shown in Figure 4. The trend and annual signals based on the least squares fitting are shown in Table 1.

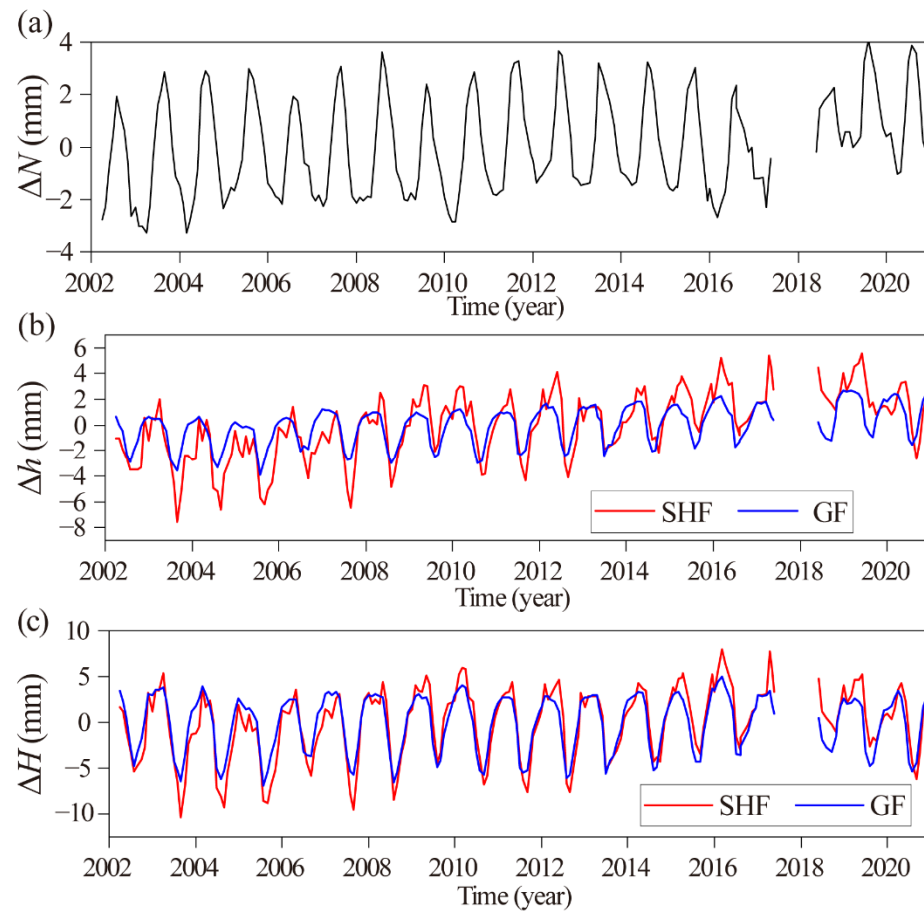


**Figure 4.** Variations of (a) geoid height, (b) surface vertical displacement and (c) height variations time series.

**Table 1.** Linear trend and annual signals based on the least squares fitting.

Time Series	Linear Trend ( $\text{mm} \cdot \text{Year}^{-1}$ )	Annual Amplitude (mm)	Annual Phase ( $^{\circ}$ )
$\Delta N$	$0.08 \pm 0.01$	$2.32 \pm 0.06$	$230.48 \pm 0.03$
$\Delta h^{\text{SHF}}$	$0.29 \pm 0.02$	$2.12 \pm 0.12$	$73.71 \pm 0.06$
$\Delta h^{\text{GF}}$	$0.12 \pm 0.01$	$1.73 \pm 0.04$	$39.79 \pm 0.02$
$\Delta H^{\text{SHF}}$	$0.21 \pm 0.02$	$4.34 \pm 0.16$	$61.57 \pm 0.04$
$\Delta H^{\text{GF}}$	$0.03 \pm 0.01$	$4.03 \pm 0.08$	$45.91 \pm 0.02$

From Figure 4, it can be seen that  $\Delta N$ ,  $\Delta h$ , and  $\Delta H$  in the QTP all show strong seasonal fluctuations, most notably annual variations. Moreover, the long-term trend is not obvious, only showing a subtle upward trend, which suggests the hydrological mass of the QTP has maintained a long-term balance during the study period. It is confirmed the hydrological loading is not the main reason for the continuous uplift observed with GRACE and GLDAS. The hydrological loading is not significant in the QTP, with the annual amplitude of about  $2.12 \pm 0.12$  and  $1.73 \pm 0.04$  mm by SHF and GF, respectively (Figure 4b). The annual phase difference between  $\Delta N$  and  $\Delta h$  is about 6 months, revealing the relationship between hydrological mass change, geoid height, and surface vertical displacement. The average  $\Delta H$  of the QTP varies significantly in different periods, for example, the difference of  $\Delta H^{\text{SHF}}$  between September 2003 and April 2017 reaches 18 mm (Figure 4c). Additionally,

$\Delta H$  reached the maximum and minimum values around February to March and August to September, respectively, and the maximum difference between the SHF, and GF is about 4 mm in the same period.

The long-term trends and annual amplitudes of  $\Delta H$  in the QTP based on the least squares fitting are shown in Figures 5 and 6, respectively. The trends of height variations in the study area are characterized by uneven spatial distribution (Figure 5), roughly bounded by block boundaries, with large differences on both sides. The trend of uplift in the southwestern part of the QTP near the Indian plate is about 1 mm/year, while the northern and eastern shows a subtle decrease (Figure 5a), which agree with the results in Duan et al. [25]. Overall,  $\Delta H^{GF}$  derived by the GLDAS hydrological model are smaller than the  $\Delta H^{SHF}$  to some degree.

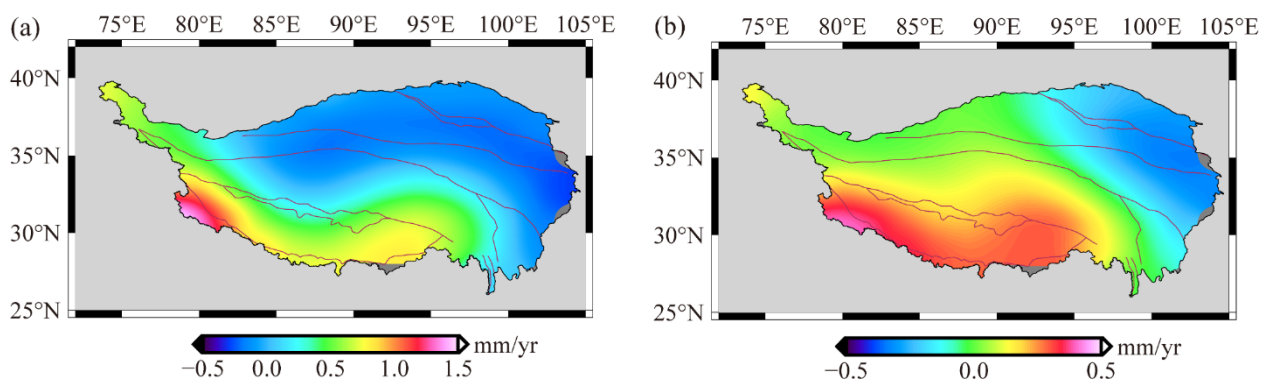


**Figure 5.** Trend of height variation derived from (a) SHF, (b) GF on the QTP, and the dark red line represents the block boundary.

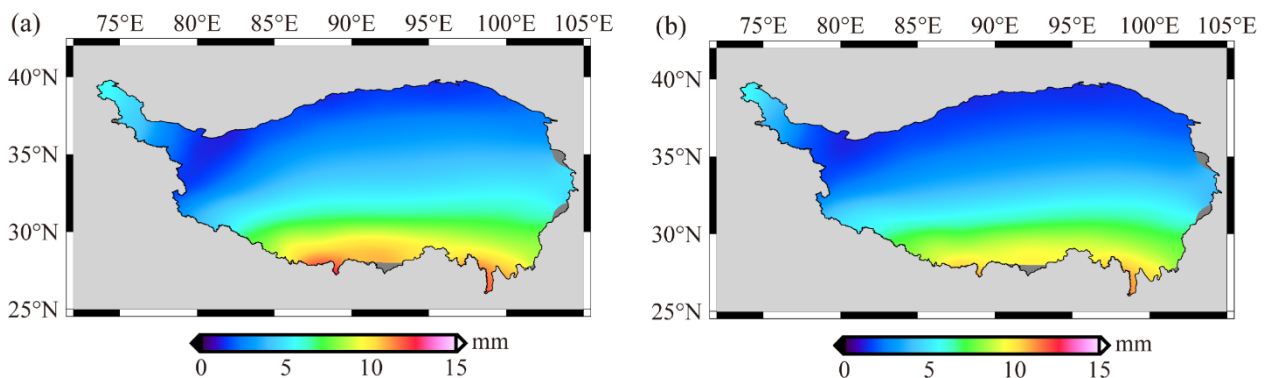


**Figure 6.** The annual amplitudes of height variation derived from (a) SHF, (b) GF on the QTP.

Figure 6 suggests there is a good agreement between the annual amplitudes of  $\Delta H$  estimated by SHF, and GF, which all show a latitudinal distribution, i.e., the annual amplitudes decrease gradually with increasing latitude. The maximum annual amplitudes of  $\Delta H^{SHF}$ , and  $\Delta H^{GF}$  are 13.06 mm, and 12.15 mm, respectively, where the maximum values are located in the southern part of the QTP, while the rest of the region is not significant less than 5 mm.

#### 4.2. Comparison of Height Variations at GPS Stations

The height derived directly from GPS is the surface vertical displacement, noted as  $\Delta h^{GPS}$  in this study. It is necessary to subtract the geoid change  $\Delta N$  from averaging  $\Delta h^{GPS}$  by each month, which converts  $\Delta h^{GPS}$  into height variations  $\Delta H^{GPS}$  based on Equation (1).

Table 2 shows the long-term trends of height variations  $\Delta H$  at GPS stations based on the least squares fitting. The long-term trends derived from GRACE (-FO) and GLDAS are fairly close to each other at some GPS stations (e.g., DLHA, QHLH, QHMY, and SCJL), but

differ considerably in most stations. GPS-derived  $\Delta H$  include not only the hydrological loading but also the effect of tectonic movements [52], which are significantly different from the results of time-varying gravity and hydrological models.

**Table 2.** Long-term trends of height variations at GPS stations.

Station	Lon. (°)	Lat. (°)	GPS Time Span (Year)	GPS (mm/Year)	SHF (mm/Year)	GF (mm/Year)
DLHA	97.38	37.38	1999.16~2021.24	0.15 ± 0.04	−0.20 ± 0.02	−0.27 ± 0.01
GSMa	102.06	34.02	2010.67~2021.24	0.61 ± 0.16	−0.24 ± 0.03	−0.34 ± 0.02
LHAS	91.1	29.66	1999.16~2021.24	0.15 ± 0.08	0.76 ± 0.03	0.30 ± 0.02
QHBM	100.74	32.93	2010.88~2021.24	0.12 ± 0.13	−0.09 ± 0.03	−0.23 ± 0.02
QHDL	98.1	36.3	2010.65~2021.24	0.58 ± 0.20	−0.23 ± 0.02	−0.31 ± 0.01
QHGC	100.13	37.33	2011.01~2021.24	0.93 ± 0.16	−0.16 ± 0.02	−0.30 ± 0.01
QLH	93.33	38.74	2010.72~2021.09	0.71 ± 0.18	−0.12 ± 0.02	−0.13 ± 0.01
QHMD	98.21	34.92	2011.18~2021.24	1.40 ± 0.19	−0.13 ± 0.02	−0.26 ± 0.02
QHME	101.4	37.47	2010.65~2021.24	1.62 ± 0.14	−0.12 ± 0.02	−0.29 ± 0.01
QHMQ	100.25	34.48	2010.64~2021.24	0.52 ± 0.17	−0.09 ± 0.02	0.10 ± 0.01
QHMY	90.8	38.48	2011.44~2021.23	0.37 ± 0.16	−0.07 ± 0.02	−0.03 ± 0.01
QH TT	92.44	34.22	2011.25~2021.23	1.28 ± 0.15	−0.01 ± 0.02	0.07 ± 0.01
QHYS	97.01	33.01	2010.66~2021.24	−0.25 ± 0.19	0.07 ± 0.03	−0.13 ± 0.02
SCDF	101.12	30.98	2011.01~2019.04	0.12 ± 0.18	−0.12 ± 0.03	−0.18 ± 0.02
SCGZ	100.02	31.61	2010.31~2021.24	0.15 ± 0.13	−0.02 ± 0.03	−0.17 ± 0.02
SCJL	101.5	29.01	2010.54~2021.23	−0.48 ± 0.16	−0.12 ± 0.03	−0.15 ± 0.02
SCLH	100.67	31.39	2010.39~2021.24	0.37 ± 0.13	−0.02 ± 0.03	−0.17 ± 0.02
SCLT	100.22	29.99	2011.27~2021.24	0.61 ± 0.13	0.03 ± 0.03	−0.09 ± 0.02
SCML	101.28	27.93	2010.50~2021.24	−0.70 ± 0.21	0.08 ± 0.04	−0.03 ± 0.03
SCXC	99.8	28.94	2010.55~2021.24	−0.19 ± 0.14	0.15 ± 0.03	−0.02 ± 0.03
XJYT	81.97	36.43	2011.13~2021.24	−0.21 ± 0.14	0.07 ± 0.02	−0.03 ± 0.01
XNIN	101.77	36.6	1999.16~2021.24	−0.04 ± 0.06	−0.19 ± 0.02	−0.33 ± 0.02
XZAR	87.18	29.27	2011.27~2021.24	−0.05 ± 0.20	0.59 ± 0.03	0.26 ± 0.02
XZBG	81.43	30.84	2011.25~2021.18	0.25 ± 0.23	1.18 ± 0.04	0.41 ± 0.03
XZCD	97.17	31.13	2010.33~2021.24	2.27 ± 0.20	0.39 ± 0.03	0.04 ± 0.02
XZCY	97.47	28.66	2010.68~2021.24	0.42 ± 0.23	0.43 ± 0.03	0.10 ± 0.03
XZDX	91.1	30.48	2011.09~2020.57	0.36 ± 0.16	0.66 ± 0.03	0.29 ± 0.02
XZGE	80.11	32.52	2010.94~2021.01	0.40 ± 0.20	0.92 ± 0.03	0.26 ± 0.02
XZNQ	92.11	31.49	2010.70~2013.41	−0.00 ± 0.44	0.56 ± 0.03	0.27 ± 0.02
XZRK	88.87	29.25	2011.44~2021.24	0.91 ± 0.17	0.61 ± 0.03	0.26 ± 0.02
XZRT	79.72	33.39	2010.82~2021.24	0.47 ± 0.14	0.81 ± 0.03	0.17 ± 0.02
XZZB	84.16	29.68	2011.38~2019.91	1.15 ± 0.26	0.76 ± 0.04	0.33 ± 0.02
XZZF	86.94	28.36	2012.40~2021.24	0.63 ± 0.27	0.73 ± 0.04	0.30 ± 0.02
YNZD	99.7	27.82	2011.00~2021.22	−0.72 ± 0.20	0.08 ± 0.04	−0.03 ± 0.03

The annual amplitude of  $\Delta H$  at the GPS stations is given in Figure 7, where the length of the arrow represents the magnitude of the annual amplitude and the angle turned clockwise from north represents the annual phase. The annual phase at 34 GPS stations is roughly located in the range of 10° to 50° (Figure 7), corresponding to the annual maximum

around January to March, and the annual phase of  $\Delta H^{\text{GPS}}$  is earlier than other results. There is a phase difference of about 25 days between the  $\Delta H^{\text{SHF}}$  derived from GRACE (-FO) time-varying gravity model with the  $\Delta H^{\text{GF}}$  estimated by GLDAS hydrological model. One possible cause of the obvious phase difference is the local groundwater-induced porous response, which is not considered in our elastic loading model and may lead to a phase shift of ground deformation [54]. The annual amplitudes of  $\Delta H$  obtained by different methods are approximately equal in the southern parts of the QTP, while  $\Delta H^{\text{GPS}}$  in western and northern parts are larger than the  $\Delta H^{\text{SHF}}$  or  $\Delta H^{\text{GF}}$ .

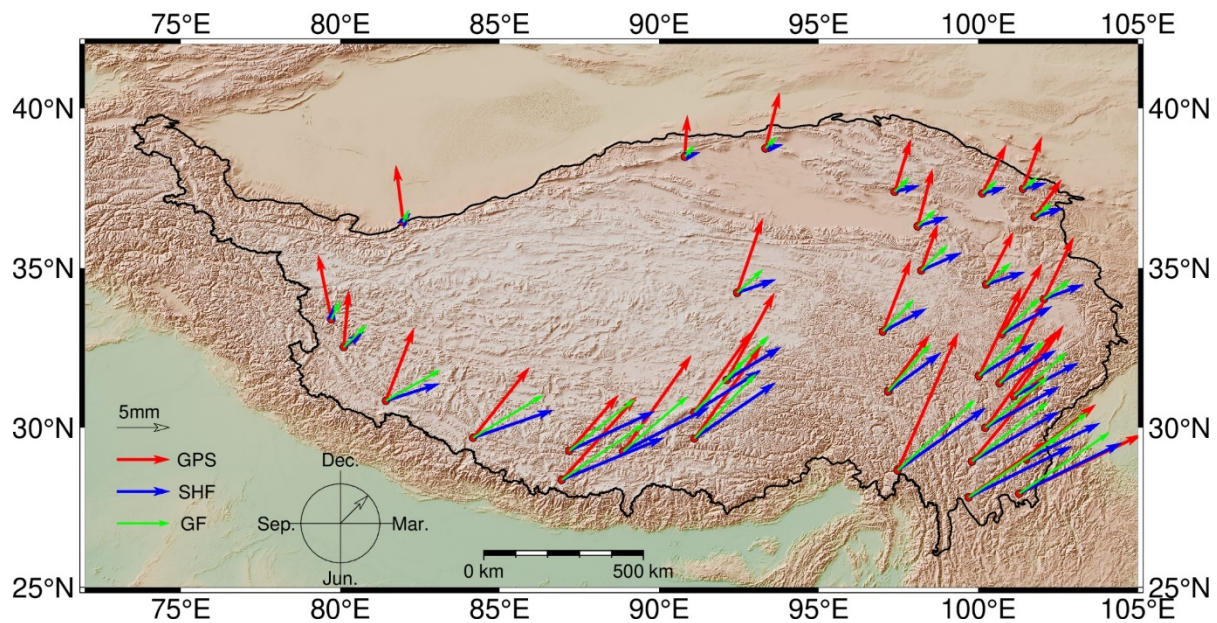


**Figure 7.** Annual amplitude and phase of height variations at 34 GPS stations. The background color represents topography.

The time series of vertical displacement with the long-term trend removed at LHAS, QHBM, SCLH, and XZCY stations are shown in Figure 8, which suggests there is the largest amplitude of  $\Delta h^{\text{GPS}}$ , while  $\Delta h^{\text{SHF}}$ , and  $\Delta h^{\text{GF}}$  have approximately equal annual amplitudes. In addition, the different results showed significant seasonal fluctuations, with the most significant annual periodic signals. Vertical displacement uplifts in winter and descends in summer. The annual peak of subsidence occurs in summer, which coincides with the time of year when the summer monsoon brings heavy precipitation and increases the surface mass loading [16]. It can be inferred that the seasonal fluctuations in the QTP are largely influenced by the hydrological loading due to precipitation, with the surface loading increasing during the summer and decreasing during the winter.

#### 4.3. Correlation Analysis of Height Variations at GPS Stations

The correlation coefficient is used to evaluate the degree of linear correlation between two time series. Figure 9 presents the correlation coefficients of  $\Delta H^{\text{GPS}}$  time series with  $\Delta H^{\text{SHF}}$ , and  $\Delta H^{\text{GF}}$ , respectively, with the long-term trend removed.  $\Delta H^{\text{GPS}}$  are positively correlated between the  $\Delta H$  estimated by the GRACE and GLDAS. Compared with the  $\Delta H^{\text{SHF}}$  (Figure 9a), the correlation coefficients of  $\Delta H^{\text{GF}}$  and  $\Delta H^{\text{GPS}}$  (Figure 9b) are larger, with the average correlation coefficients of 0.70, and 0.82 between the SHF/GF and GPS, respectively, which indicates that GPS, GRACE (-FO), and the GLDAS detect some degree of the same geophysical signal while mixing the non-hydrological signal in the GPS height. The correlation strength varies among GPS stations, and the correlation is stronger in the southern part of the QTP near the Indian and Myanmar plates than in the northern part, which may be due to the more significant hydrological loading caused by the whole TWS in the southern part.

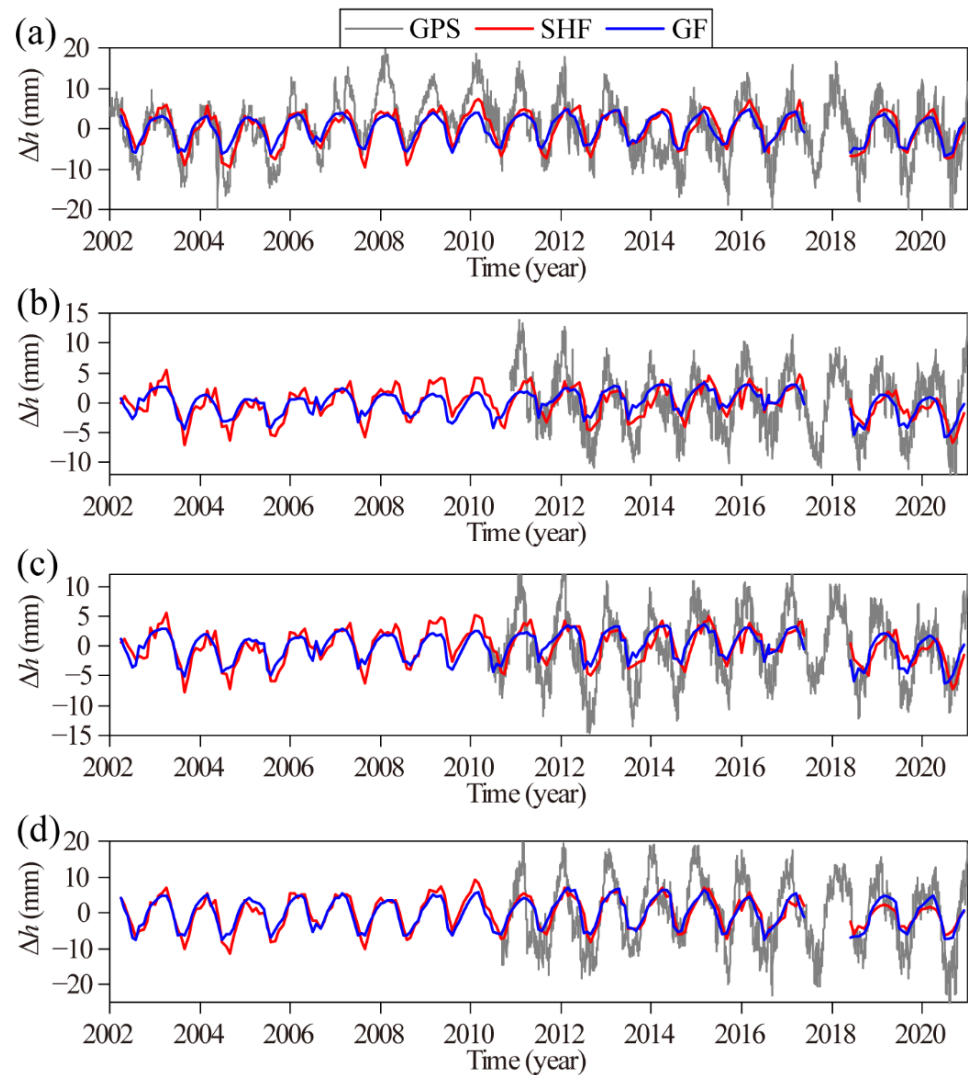


**Figure 8.** Time series of vertical displacement (with the long-term trend removed), (a) LHAS, (b) QHBM, (c) SCLH, (d) XZCY.

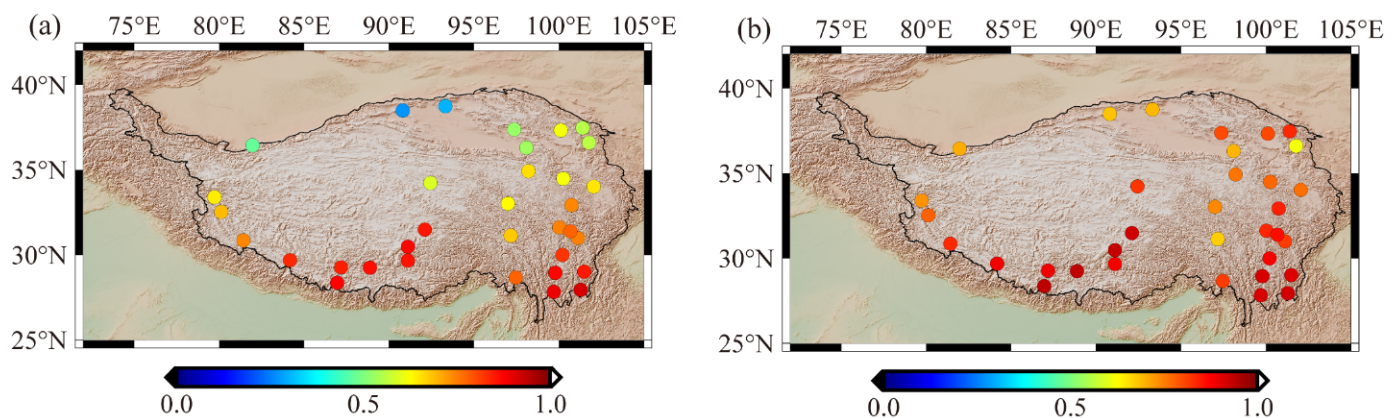


**Figure 9.** Correlation coefficient of height variation, (a) GPS and SHF, (b) GPS and GF. The background color represents topography.

#### 4.4. Wavelet Coherence analysis of Height Variations at GPS Stations

Since correlation analysis is sensitive to phase, but cannot evaluate the consistency of amplitudes. The wavelet coherence analysis [55] could characterize the signal in the

spatial and frequency domains, so the continuous wavelet transform (CWT) is used to analyze relationships in the time-frequency space of height variations derived from GPS, GRACE (-FO), and GLDAS. The method of wavelet coherence analysis can be found in Grinsted et al. [55].

Station LHAS is used as an example for wavelet analysis in this paper. Figure 10 shows the CWT power spectrum of  $\Delta H^{\text{GPS}}$  with  $\Delta H^{\text{SHF}}$  ( $\Delta H^{\text{GF}}$ ) for the LHAS station, which indicates that the height variations estimated by different methods have a resonance period of 8–16 months (0.7–1.3 years) within the study period and pass the significance test. It suggests that  $\Delta H$  of LHAS station have significant annual period signals, while the other periods are not significant. CWT reveals the oscillation period of the multi-time scale transform characteristics of the single time series. To analyze the characteristics of the mutual period between height variations derived from GRACE (-FO), GLDAS with GPS, Cross wavelet transform (XWT), and wavelet coherence (WTC) are performed.

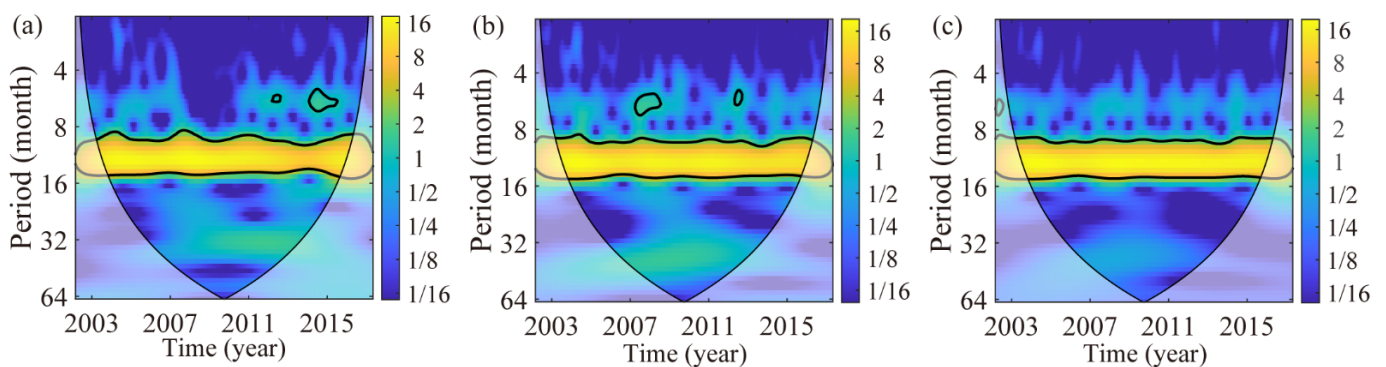


**Figure 10.** Continuous wavelet (CWT) power spectrum of height variations derived from (a) GPS, (b) SHF and (c) GF at LHAS station.

XWT reveals the phase relationship in the high energy region common to both data within the time-frequency space. From Figure 11, it can be seen that  $\Delta H^{\text{GPS}}$  exists a period of 8 to 16 months (0.7–1.3 years) with  $\Delta H^{\text{SHF}}$  ( $\Delta H^{\text{GF}}$ ) and passes the significance test. Most arrows in this period face to the right, indicating the same phase. In addition, there is a semi-annual periodic signal of some energy (2012 and 2014), but the energy is not significant.

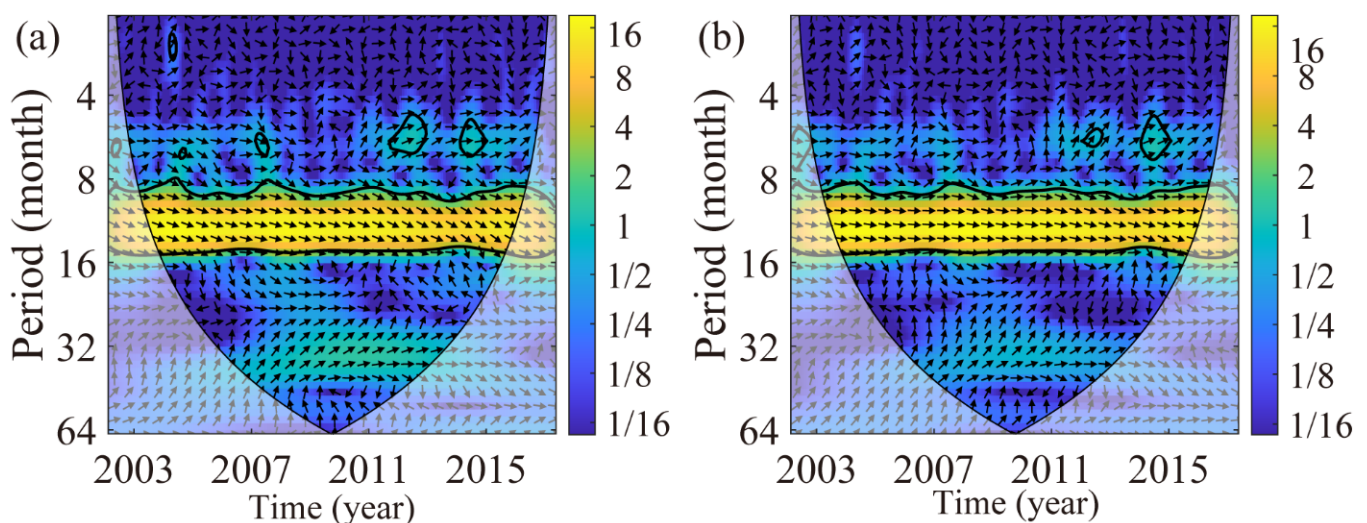


**Figure 11.** Cross wavelet transform (XWT) of height variations derived from (a) GPS and SHF, (b) GPS and GF at LHAS station. The relative phase relationship is shown as arrows (with in-phase pointing right, anti-phase pointing left, and GPS leading SHF/GF by 90° pointing straight down).

WTC compensates for the deficiency of XWT in the low-energy region and estimates the correlation between the two datasets. Figure 12 shows that in addition to the annual period (0.7–1.3 years), there are also semi-annual and 32-month (2.7 year) periods between  $\Delta H$  derived from GPS and GRACE/GLDAS. The 2.7-year periodic oscillation between  $\Delta H^{\text{GPS}}$  and  $\Delta H^{\text{SHF}}$  passed the significance test in the whole period, indicating that  $\Delta H$  detected by GRACE (-FO) in the high-frequency part is the main factor of the GPS height variations. The 2.7-year period also exists between GPS and GF from 2002 to 2011, and the specific reasons for this period need further analysis.

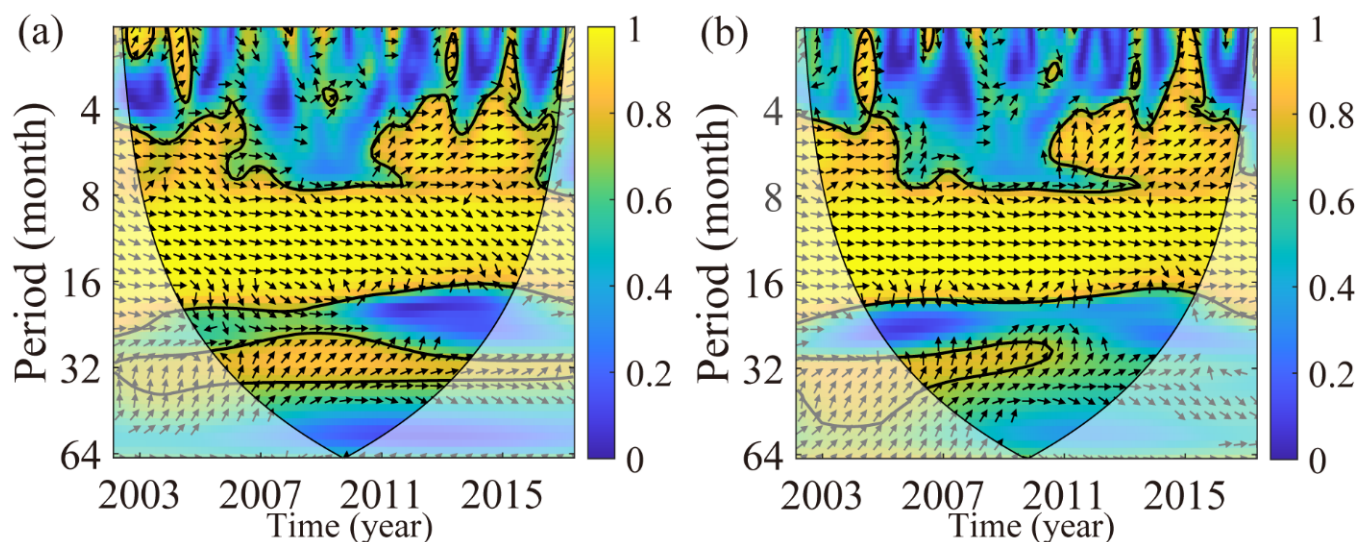


**Figure 12.** Wavelet coherence (WTC) of height variations derived from (a) GPS and SHF, (b) GPS and GF at LHAS station. The meaning of arrows the same as in Figure 11.

Height variations derived from different datasets mainly present the annual periodic oscillation signal. To quantitatively express the relative phase relationship between two signals [56], the average values of WTC-based semblance (Figure 13a) and average relative phase angle (Figure 13b) are estimated.

The average values of WTC-based semblance for most GPS sites are close to 1 (Figure 13a), which indicates the height variations derived from GRACE (-FO) or GLDAS almost explain GPS height in annual periodic signals, but not completely. In addition, the average WTC-based semblance of GPS and SHF is significantly lower than that of GPS and GF at stations DLHA, QHLH, QHMY, XINI, XZGE, and XZRT, which may be since groundwater loading is not the main factor causing height variations at these stations. The average semblances of the annual periodicity for most of the other stations are  $\sim 0.98$ , showing there is a strong geophysical coherence between the height variations derived by GPS and GRACE/GLDAS. After removing NTAL, NTOL, and bedrock thermal expansion, the hydrological mass migration is the main reason for the seasonal height variations of the GPS.

The average relative phase angle of  $\Delta H^{\text{GPS}}$  is earlier than other results, and that estimated by GPS and GF is closer, whose difference is smaller than GPS and SHF (Figure 13b). In this regard, we find that the height variations derived from GLDAS are more consistent with GPS in the range of annual fluctuation.

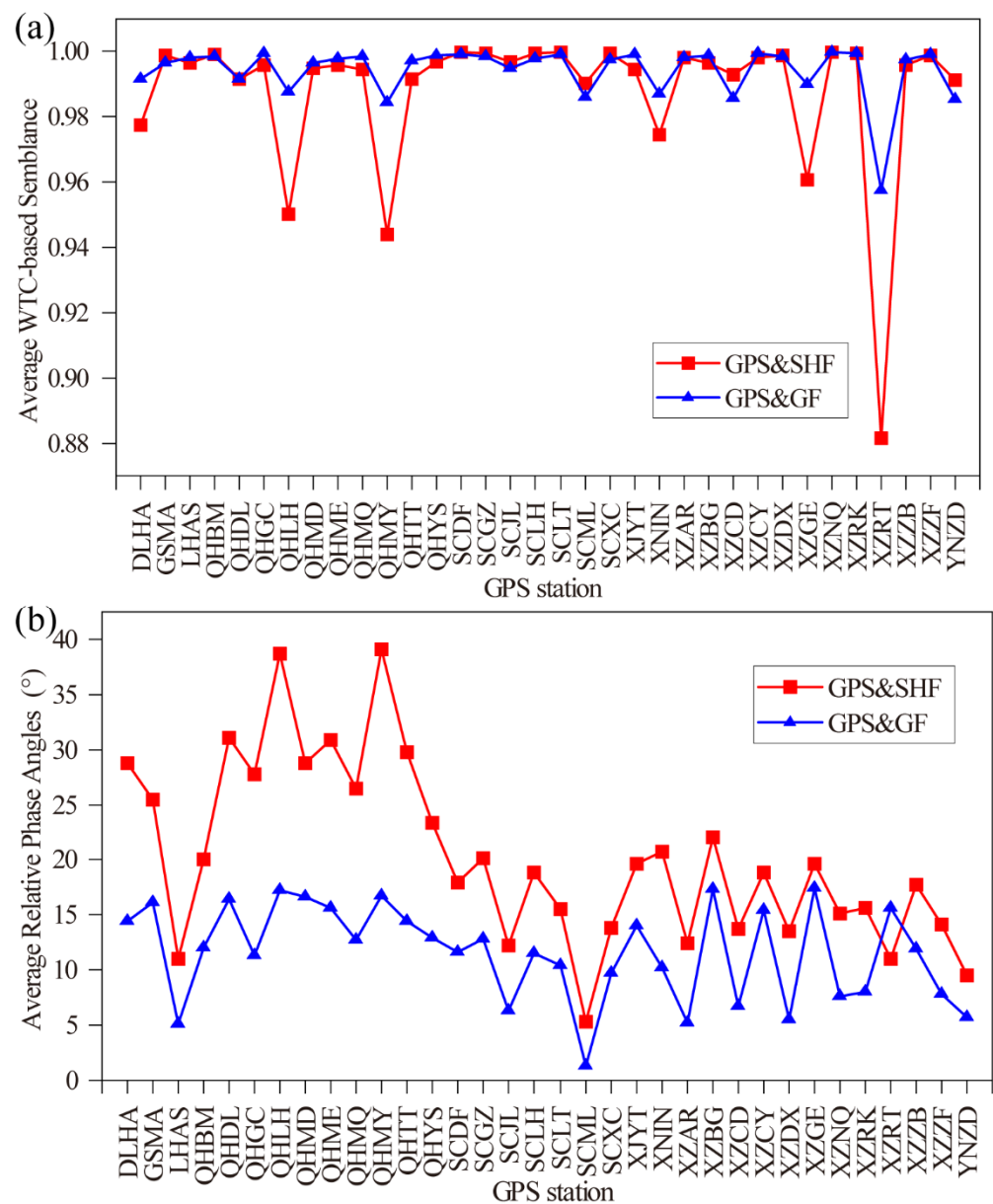


**Figure 13.** (a) The average values of the WTC-based semblance that is outside the COI at the period closest to 1 year for the 34 stations, (b) the average relative phase angles between GPS and SHF/GF time series of height variations from the 34 stations.

## 5. Discussions

### 5.1. Differences in Height Variations Derived from GRACE (-FO) and GLDAS

In this paper, GRACE (-FO) and GLDAS are used to study the vertical displacement and height change in the QTP. From Section 4.1, it can be seen that the SHF and GF methods could reveal the long-term trend and seasonal fluctuations of height variations in the QTP, but there are still some differences between the different results. Figure 4b,c show that the annual amplitudes of the height derived from GRACE (-FO) are larger than those from GLDAS. The reason may be that GLDAS only contributes to 0–2 m soil moisture canopy water, and snow to hydrological mass changes, ignoring the effort of deep subsoil water, groundwater, lakes, wetlands, etc. While GRACE (-FO) considers gravity as hydrological mass after removing atmospheric and non-tidal oceanic influences and integrating various factors such as groundwater and deep soil water, therefore the amplitude of height variations estimated by GRACE (-FO) is larger than that of GLDAS.

We estimate groundwater by TWS derived from GRACE minus soil moisture and snow water equivalent obtained from GLDAS based on regional water balance [13,19]. The groundwater of the QTP accounts for ~28% of the TWS. To be clear, the proportion of groundwater is overestimated because we ignored surface water due to data limitations. The effect of groundwater on height variations was not modelled separately because we focused on the whole hydrological loading. In general, it can be concluded that the discrepancy in height variations between GRACE (-FO) and GLDAS is mainly due to the different technical models.

In addition, the GRACE mission had some measuring and processing errors, which may related to truncation; van Dam et al. (2007) argue that the error of the GRACE gravity model is less than the millimeter level [57]. The inversion of height variations by GRACE (-FO) has certain drawbacks, which reflect the mass change at a large scale and lacks spatial resolution for the influence of small-scale material sources. There will be a large bias in areas dominated by groundwater loading because the displacement caused by groundwater is in the opposite direction of surface loading [7]. The discrepancies between GRACE and GLDAS are mainly related to their uncertainty, including initial conditions, climate forcing, land cover input, model structure, etc. [58]. There are still some unmodeled errors, such as seasonal variations in immaterial gravity loading (temperature and magnetic fields), whose effects need to be further explored.

## 5.2. Quantitative Assessment of Hydrological Loading on GPS Height

To quantitatively assess the effectiveness of removing the hydrological loadings in GPS vertical displacement by GRACE (-FO) and GLDAS, the weighted root-mean-square (WRMS) and its reduction could be estimated, which is defined by Equations (3) and (4) in He et al. (2017) [59].

The  $WRMS_{\text{reduction}}$  reflects the consistency of  $\Delta H^{\text{GPS}}$  and  $\Delta H^{\text{SHF}}$  ( $\Delta H^{\text{GF}}$ ) in the annual periodic signals and the closer its value is to 1 indicates that the period term of the two fits is closer to each other. Figure 14 shows the  $WRMS_{\text{reduction}}$  ratio by removing the GRACE (-FO) and GLDAS-derived height variations from GPS-derived seasonal signals at the QTP 34 GPS stations. The average  $WRMS_{\text{reduction}}$  between GPS and SHF/GF is 29% (Figure 14a), and 37% (Figure 14b), respectively, which indicates the effect of GPS removed by GF methods is better than that of SHF. The height variations  $\Delta H^{\text{GF}}$  estimated by GLDAS is more consistent with the annual signals of  $\Delta H^{\text{GPS}}$ , therefore the improvement of hydrological loading by GLDAS in GPS height is better.

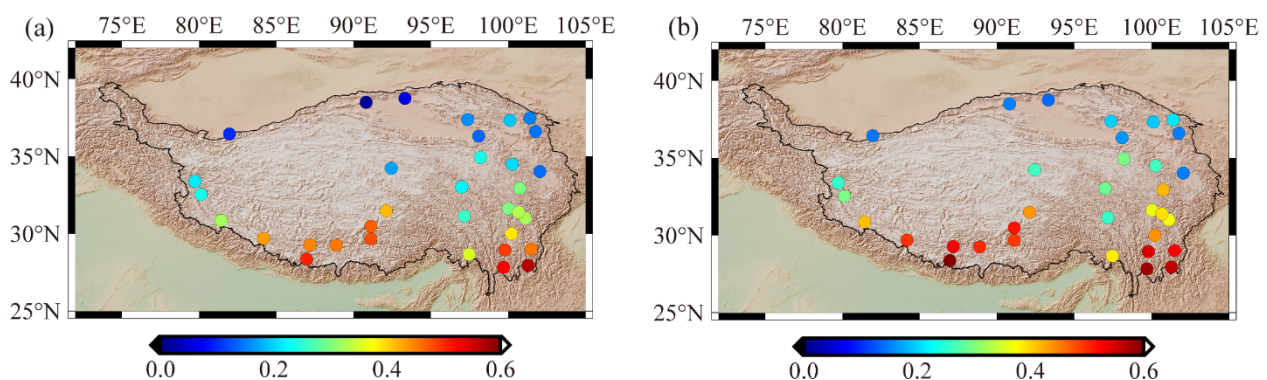


**Figure 14.**  $WRMS_{\text{reduction}}$  for 34 GPS stations when (a) SHF- (b) GF-derived seasonal signals removed reduction from GPS vertical displacement time series. The background color represents topography.

Comparing Figure 9 with Figure 14, it can be seen that there is a certain spatial correlation between the correlation coefficient and the  $WRMS_{\text{reduction}}$ , which are significantly larger in the south of the QTP than in other regions. The hydrological loading is the dominant factor influenced by the summer monsoon in the southern, where the GRACE (-FO) or GLDAS seasonal signals with GPS show better consistency. While the north of the study

area, which is closer to the interior, is less influenced by the summer monsoon, where the correlation and consistency are significantly lower.

### 5.3. Tectonic Movement Rates

The height variations derived from GPS include not only surface mass loading but also the effects of internal tectonic movements [5]. The surface loading in GPS heights needs to be deducted to reveal the tectonic movements of the QTP. There are some discussions on comparing or combining vertical displacement from GRACE and GPS to study the water cycle and tectonic movements [26,27,30,31,51,55,56]. However, the use of GRACE to remove the hydrological loading in GPS may be imperfect due to differences in observational patterns. Zhang et al., argued that the loading differences between GRACE and GPS are significant both on a regional average and at a single point, and directly using GRACE to remove the seasonal signal from GPS to study the remaining tectonic signal is challenging [60]. In contrast, the results in Figure 14 from the GRACE (-FO) and GLDAS hydrological models to remove the hydrological loading signal from GPS, respectively, show a higher  $WRMS_{\text{reduction}}$  by GLDAS.

As shown in Section 5.2,  $WRMS$  of the height variations of 34 GPS stations are reduced to different degrees by removing the hydrological loading in GPS height with GRACE (-FO) and GLDAS, and  $WRMS$  by the GF is reduced to the greatest extent. Therefore, the hydrological loading in the GPS height variations is removed by the  $\Delta h^{\text{GF}}$  and the remaining signal is considered to be caused by the tectonic motion.

Figure 15 shows the vertical rates of tectonic motion of GPS station with the loading effects removed (GPS height subtracts GLDAS-derived hydrological loading based on the GF). Except for the subsidence of XZLNQ, XINI, XJYT, YNZD, and SCML, all other stations are uplifting at a rate of 0.06 mm/year–1.97 mm/year in the study area (Figure 15). The uplift rate of the main Main Himalaya Thrust and the Karakorum-Jiali Fault Zone is about 1 mm/year, and individual GPS stations (e.g., XZLNQ) show a subsidence component, which may be related to the rebound fault activity or local collapse of the margin. The uplift rate of the northeastern part is not significant, while the stations near the Jinsha River-Honghe Fault Zone uplift at a rate of 0.2–1 mm/year, except for the SCML station, which indicates a significant subsidence rate.

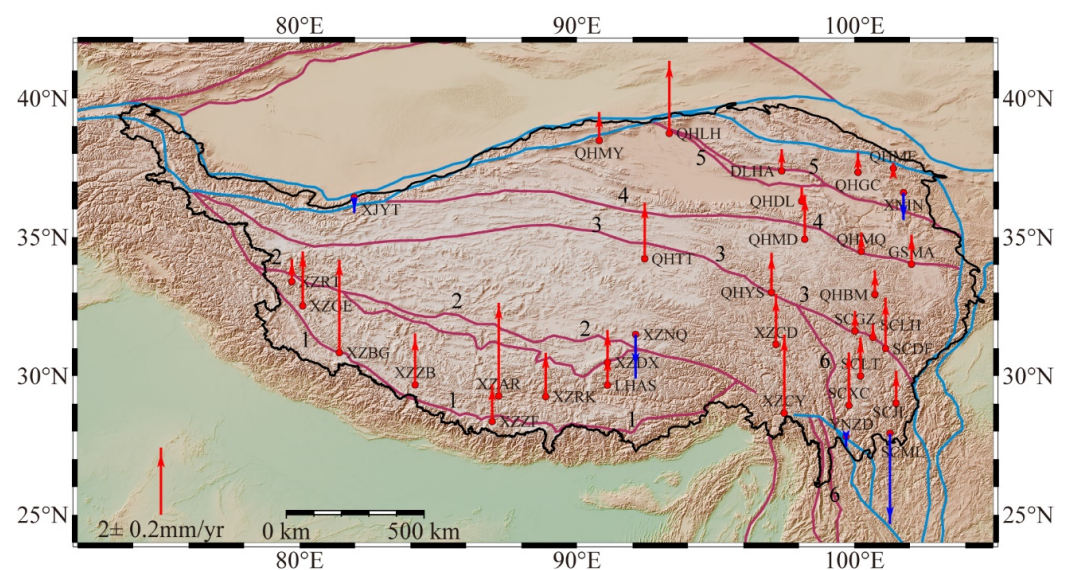


**Figure 15.** Vertical tectonic motion with the hydrological loading effects removed, red and blue arrows indicate uplift and subsidence, respectively, the dark red and blue lines are the block boundaries. 1. Main Himalaya Thrust, 2. Karakorum-Jiali Fault Zone, 3. Mani-Yushu-Shinshui River Fault Zone, 4. Kunlun-Maqen Fault Zone, 5. Altun-Haiyuan Fault Zone, 6. Jinsha River-Red River Fault Zone. The background color represents topography.

The deformation detected by GPS is mainly affected by the local loading around 100–200 km. Some faults do not show a unified tectonic movement, but are composed of multiple distinct motions, e.g., Jinsha River-Honghe Fault Zone. The northern part of the Jinsha River-Honghe Fault Zone, represented by SCLT and SCXC, shows a unified uplift trend, which is caused by active subduction of the Yangtze Craton [26]. While the southern part, represented by SCML, shows a subsidence trend attributed to the asthenosphere. It is the same result as that of Hao et al. [61], who argued that the assumption of uniform extension does not explain the subsidence of southern Sichuan–Yunnan fragment.

## 6. Conclusions

The crust of Tibetan Plateau is still uplifting and thickening nowadays which was revealed by the geological and tectonic results. Based on the GRACE (-FO) time-varying gravity model, GLDAS, and GPS vertical coordinate time series, the height variations (above the geoid) of the QTP from 2002 to 2020 are obtained in this study. The overall height variations caused by hydrological mass on QTP during the study period show a slight increase, which indicates hydrological loading is not the main cause of the uplifting observed with GRACE.

The seasonal term (e.g., annual and semi-annual period) caused by hydrological loading is included in the GPS vertical displacement, which needs to be eliminated to reveal the tectonic motion. In terms of hydrological load on GPS height, GLDAS-derived is more consistent with GPS height than that from GRACE (-FO) based on  $WRMS_{reduction}$ . The vertical tectonic motion of GPS stations is estimated with the GLDAS-derived hydrological loading removed. Most stations are uplifted at the rate of 0.06mm/year–1.97 mm/year. To explain the uplift rate of QTP in more detail, more intensive GPS continuous stations need to be analyzed, and more accurate physical models of surface vertical displacement such as hydrological and atmospheric loads and bedrock thermal expansion also need to be considered. Overall, the approach of estimating height variations and tectonic motion in this paper provides a valuable reference for the study of other earthquake-prone areas such as Japan, Chile, etc., and engineering works, e.g., deformation monitoring of constructions.

**Author Contributions:** Conceptualization, writing—original draft preparation, writing—review and editing and methodology, T.S., J.G. and H.Y.; software, T.S.; validation, J.G. and X.L.; formal analysis, X.C. and B.J.; resources, J.G. and H.Y.; data curation, T.S., X.C. and B.J.; funding acquisition, J.G., X.C. and B.J. All authors have read and agreed to the published version of the manuscript.

**Funding:** This research is supported by the National Natural Science Foundation of China (Grant No. 41874091, 42174041 and 41774001), the Autonomous and Controllable Special Project for Surveying and Mapping of China (Grant No. 816-517), and the SDUST Research Fund (Grant No. 2014TDJH101).

**Data Availability Statement:** The datasets generated during and/or analyzed during the current study are available from the corresponding author on reasonable request.

**Acknowledgments:** We are very grateful to CSR for providing GRACE data and NASA for providing GLDAS model. The GPS data used in this paper are primarily from the CMONOC, and we express our gratitude and thanks to participants for constructing the network and making the GPS measurements.

**Conflicts of Interest:** The authors declare no conflict of interest.

## References

1. Molnar, P.; Tapponnier, P. Cenozoic tectonics of Asia: Effects of a continental collision. *Science* **1975**, *189*, 419–426. [[CrossRef](#)] [[PubMed](#)]
2. Sun, W.; Wang, Q.; Li, H.; Wang, Y.; Okubo, S.; Shao, D.; Liu, D.; Fu, G. Gravity and GPS measurements reveal mass loss beneath the Tibetan Plateau: Geodetic evidence of increasing crustal thickness. *Geophys. Res. Lett.* **2009**, *36*, L02303. [[CrossRef](#)]
3. Pan, Y.; Hammond, W.C.; Ding, H.; Mallick, R.; Jiang, W.; Xu, X.; Shum, C.K.; Shen, W. GPS imaging of vertical bedrock displacements: Quantification of two-dimensional vertical crustal deformation in China. *J. Geophys. Res. Solid Earth* **2021**, *126*, e2020JB020951. [[CrossRef](#)]

4. Fuhrmann, T.; Westerhaus, M.; Zippelt, K.; Heck, B. Vertical displacement rates in the Upper Rhine Graben area derived from precise leveling. *J. Geod.* **2014**, *88*, 773–787. [[CrossRef](#)]
5. Bawden, G.W.; Thatcher, W.; Stein, R.S.; Hudnut, K.W.; Peltzer, G. Tectonic contraction across Los Angeles after removal of groundwater pumping effects. *Nature* **2001**, *412*, 812–815. [[CrossRef](#)] [[PubMed](#)]
6. Devoti, R.; Esposito, A.; Pietrantonio, G.; Pisani, A.R.; Riguzzi, F. Evidence of large scale deformation patterns from GPS data in the Italian subduction boundary. *Earth Planet. Sci. Lett.* **2011**, *311*, 230–241. [[CrossRef](#)]
7. Tan, W.; Dong, D.; Chen, J.; Wu, B. Analysis of systematic differences from GPS-measured and GRACE-modeled deformation in Central Valley, California. *Adv. Space Res.* **2016**, *57*, 19–29. [[CrossRef](#)]
8. Liang, S.; Gan, W.; Shen, C.; Xiao, G.; Liu, J.; Chen, W.; Ding, X.; Zhou, D. Three-dimensional velocity field of present-day crustal motion of the Tibetan Plateau derived from GPS measurements. *J. Geophys. Res. Solid Earth* **2013**, *118*, 5722–5732. [[CrossRef](#)]
9. Xing, L.; Sun, W.; Li, H.; Yang, G. Present-day crust thickness increasing beneath the Qinghai-Tibetan Plateau by using geodetic data at Lhasa Station. *Acta Geod. Cartogr. Sin.* **2011**, *40*, 41–44.
10. Van Camp, M.; de Viron, O.; Avouac, J.P. Separating climate-induced mass transfers and instrumental effects from tectonic signal in repeated absolute gravity measurements. *Geophys. Res. Lett.* **2016**, *43*, 4313–4320. [[CrossRef](#)]
11. Chen, Z.; Chen, S.; Zhang, B.; Wang, L.; Shi, L.; Lu, H.; Liu, J.; Xu, W. Uncertainty Quantification and Field Source Inversion for the Continental-Scale Time-Varying Gravity Dataset: A Case Study in SE Tibet, China. *Pure Appl. Geophys.* **2022**. [[CrossRef](#)]
12. Tapley, B.D.; Bettadpur, S.; Watkins, M.; Reigber, C. The gravity recovery and climate experiment: Mission overview and early results. *Geophys. Res. Lett.* **2004**, *31*, L09607. [[CrossRef](#)]
13. Othman, A.; Abdelrady, A.; Mohamed, A. Monitoring Mass Variations in Iraq Using Time-Variable Gravity Data. *Remote Sens.* **2022**, *14*, 3346. [[CrossRef](#)]
14. Rodell, M.; Velicogna, I.; Famiglietti, J.S. Satellite-based estimates of groundwater depletion in India. *Nature* **2009**, *460*, 999–1002. [[CrossRef](#)]
15. Guo, J.; Mu, D.; Liu, X.; Yan, H.; Sun, Z.; Guo, B. Water storage changes over the Tibetan Plateau revealed by GRACE mission. *Acta Geophys.* **2016**, *64*, 463–476. [[CrossRef](#)]
16. Liu, X.; Zhao, N.; Guo, J.; Sun, Y.; Guo, B.; Mou, N. Equivalent water height changes over Qinghai-Tibet Plateau determined from GRACE with an independent component analysis approach. *Arab. J. Geosci.* **2020**, *13*, 179. [[CrossRef](#)]
17. Goncalves, J.; Petersen, J.; Deschamps, P.; Hamelin, B.; Baba-Sy, O. Quantifying the modern recharge of the “fossil” Sahara aquifers. *Geophys. Res. Lett.* **2013**, *40*, 2673–2678. [[CrossRef](#)]
18. Voss, K.A.; Famiglietti, J.S.; Lo, M.H.; de Linage, C.; Rodell, M.; Swenson, S.C. Groundwater depletion in the Middle East from GRACE with implications for transboundary water management in the Tigris-Euphrates-Western Iran region. *Water Resour. Res.* **2013**, *49*, 904–914. [[CrossRef](#)]
19. Abhishek; Kinouchi, T.; Sayama, T. A comprehensive assessment of water storage dynamics and hydroclimatic extremes in the Chao Phraya River Basin during 2002–2020. *J. Hydrol.* **2021**, *603*, 126868. [[CrossRef](#)]
20. Mohamed, A.; Abdelrahman, K.; Abdelrady, A. Application of Time-Variable Gravity to Groundwater Storage Fluctuations in Saudi Arabia. *Front. Earth Sci.* **2022**, *10*, 873352. [[CrossRef](#)]
21. Shi, T.; Liu, X.; Mu, D.; Li, C.; Guo, J.; Xing, Y. Reconstructing gap data between GRACE and GRACE-FO based on multi-layer perceptron and analyzing terrestrial water storage changes in the Yellow River basin. *Chin. J. Geophys.* **2022**, *65*, 2448–2463.
22. Geruo, A.; Wahr, J.; Zhong, S. Computations of the viscoelastic response of a 3-D compressible Earth to surface loading: An application to Glacial Isostatic Adjustment in Antarctica and Canada. *Geophys. J. Int.* **2013**, *192*, 557–572.
23. Feng, W.; Shum, C.K.; Zhong, M.; Pan, Y. Groundwater Storage Changes in China from Satellite Gravity: An Overview. *Remote Sens.* **2018**, *10*, 674. [[CrossRef](#)]
24. Farrell, W.E. Deformation of the Earth by surface loads. *Rev. Geophys.* **1972**, *10*, 761–797. [[CrossRef](#)]
25. Duan, H.; Kang, M.; Wu, S.; Chen, L.; Jiao, J. Uplift rate of the Tibetan Plateau constrained by GRACE time-variable gravity field. *Chin. J. Geophys.* **2020**, *63*, 4345–4360.
26. Pan, Y.; Shen, W.; Hwang, C.; Liao, C.; Zhang, T.; Zhang, G. Seasonal mass changes and crustal vertical deformations constrained by GPS and GRACE in Northeastern Tibet. *Sensors* **2016**, *16*, 1211. [[CrossRef](#)]
27. Van Dam, T.; Wahr, J.M. Displacements of the earth’s surface due to atmospheric loading: Effects on gravity and baseline measurements. *J. Geophys. Res.* **1987**, *92*, 1281–1286. [[CrossRef](#)]
28. Zou, R.; Wang, Q.; Freymueller, J.T.; Poutanen, M.; Cao, X.; Zhang, C.; Yang, S.; He, P. Seasonal hydrological loading in southern Tibet detected by joint analysis of GPS and GRACE. *Sensors* **2015**, *15*, 30525–30538. [[CrossRef](#)]
29. Liu, J.; Fang, J.; Li, H.; Cui, R.; Chen, M. Secular variation of gravity anomalies within the Tibetan Plateau derived from GRACE data. *Chin. J. Geophys.* **2015**, *58*, 3496–3506.
30. Zhang, T.; Shen, Z.; He, L.; Shen, W.; Li, W. Strain Field Features and Three-Dimensional Crustal Deformations Constrained by Dense GRACE and GPS Measurements in NE Tibet. *Remote Sens.* **2022**, *14*, 2638. [[CrossRef](#)]
31. Jiao, J.; Zhang, Y.; Yin, P.; Zhang, K.; Wang, Y.; Bilker-Koivula, M. Changing Moho Beneath the Tibetan plateau revealed by GRACE observations. *J. Geophys. Res. Solid Earth* **2019**, *124*, 5907–5923. [[CrossRef](#)]
32. CSR Release-06 GRACE Level-2 Data Products. Available online: <https://www2.csr.utexas.edu/grace/RL06.html> (accessed on 19 April 2022).

33. Abhishek; Kinouchi, T.; Abolafia-Rosenzweig, R.; Ito, M. Water Budget Closure in the Upper Chao Phraya River Basin, Thailand Using Multisource Data. *Remote Sens.* **2022**, *14*, 173. [[CrossRef](#)]
34. Sun, Y.; Riva, R.; Ditmar, P. Optimizing estimates of annual variations and trends in geocenter motion and J2 from a combination of GRACE data and geophysical models. *J. Geophys. Res. Solid Earth* **2016**, *121*, 8352–8370. [[CrossRef](#)]
35. Loomis, B.D.; Rachlin, K.E.; Wiese, D.N.; Landerer, F.W.; Luthcke, S.B. Replacing GRACE/GRACE-FO C30 with Satellite Laser Ranging: Impacts on Antarctic ice sheet mass change. *Geophys. Res. Lett.* **2020**, *47*, e2019GL085488. [[CrossRef](#)]
36. Peltier, W.R.; Argus, D.F.; Drummond, R. Comment on “An assessment of the ICE-6G\_C (VM5a) glacial isostatic adjustment model” by Purcell et al. *J. Geophys. Res. Solid Earth* **2018**, *123*, 2019–2028. [[CrossRef](#)]
37. Horvath, A.; Murböck, M.; Roland, P.; Horvath, M. Decorrelation of GRACE time variable gravity field solutions using full covariance information. *Geosciences* **2018**, *8*, 323. [[CrossRef](#)]
38. Rodell, M.; Houser, P.R.; Jambor, U.; Gottschalck, J.; Mitchell, K.; Meng, C.J.; Aresnault, K.; Cosgrove, B.; Radakovich, J.; Bosilovich, M.; et al. The global land data assimilation system. *Bull. Am. Meteorol. Soc.* **2004**, *85*, 381–394. [[CrossRef](#)]
39. King, R.; Bock, Y. *Documentation for the GAMIT GPS Analysis Software*; Massachusetts Institute of Technology: Cambridge, MA, USA, 2000. Available online: <https://www-gpsg.mit.edu/~simon/gtgk/GAMIT.pdf> (accessed on 24 April 2022).
40. Liu, N.; Dai, W.; Santerre, R.; Kuang, C. A MATIAB-based Kriged Kalman Filter software for interpolating missing data in GNSS coordinate time series. *GPS Solut.* **2018**, *22*, 25. [[CrossRef](#)]
41. Gelaro, R.; McCarty, W.; Suarez, M.J.; Todling, R.; Molod, A.; Takacs, L.; Randles, C.A.; Darmenov, A.; Bosilovich, M.G.; Reichle, R.; et al. The Modern-Era Retrospective Analysis for Research and Applications, Version 2 (MERRA-2). *J. Clim.* **2017**, *30*, 5419–5454. [[CrossRef](#)]
42. Jungclaus, J.H.; Fischer, N.; Haak, H.; Lohmann, K.; Marotzke, J.; Matei, D.; Mikolajewicz, U.; Notz, D.; von Storch, J.S. Characteristics of the ocean simulations in the Max Planck Institute Ocean Model (MPIOM) the ocean component of the MPI-Earth system model. *J. Adv. Model. Earth Syst.* **2013**, *5*, 422–446. [[CrossRef](#)]
43. Petrov, L. The International Mass Loading Service. In *REFAG 2014*; Van Dam, T., Ed.; International Association of Geodesy Symposia Series; Springer: Berlin/Heidelberg, Germany, 2014; Volume 146, pp. 79–83.
44. Xu, X.; Dong, D.; Fang, M.; Zhou, Y.; Wei, N. Contributions of Thermoelastic Deformation to Seasonal Variations in GPS Station Position. *GPS Solut.* **2017**, *21*, 1265–1274. [[CrossRef](#)]
45. Dong, D.; Fang, P.; Bock, Y.; Cheng, M.; Miyazaki, S. Anatomy of apparent seasonal variations from GPS derived site position time series. *J. Geophys. Res. Solid Earth* **2002**, *107*, 2075. [[CrossRef](#)]
46. Peng, S.; Ding, Y.; Liu, W.; Li, Z. 1 km monthly temperature and precipitation dataset for China from 1901 to 2017. *Earth Syst. Sci. Data* **2019**, *11*, 1931–1946. [[CrossRef](#)]
47. Heiskanen, W.A.; Moritz, H. *Physical Geodesy*; Freeman & Co.: San Francisco, CA, USA, 1967.
48. Wahr, J.M.; Molenaar, M.; Bryan, F. Time variability of the Earth’s gravity field: Hydrological and oceanic effects and their possible detection using GRACE. *J. Geophys. Res. Solid Earth* **1998**, *103*, 30205–30229. [[CrossRef](#)]
49. Dziewonski, A.M.; Anderson, D.L. Preliminary reference Earth model. *Phys. Earth Planet. Inter.* **1981**, *25*, 297–356. [[CrossRef](#)]
50. Wang, H.; Xiang, L.; Jia, L.; Jiang, L.; Wang, Z.; Hu, B.; Gao, P. Load Love numbers and Green’s functions for elastic Earth models PREM, iasp91, ak135, and modified models with refined crustal structure from Crust 2.0. *Comput. Geosci.* **2012**, *49*, 190–199. [[CrossRef](#)]
51. Godah, W.; Ray, J.D.; Szelachowska, M.; Krynski, J. The Use of National CORS Networks for Determining Temporal Mass Variations within the Earth’s System and for Improving GRACE/GRACE-FO Solutions. *Remote Sens.* **2020**, *12*, 3359. [[CrossRef](#)]
52. Chanard, K.; Avouac, J.P.; Ramillien, G.; Genrich, J. Modeling deformation induced by seasonal variations of continental water in the Himalaya region: Sensitivity to Earth elastic structure. *J. Geophys. Res. Solid Earth* **2014**, *119*, 5097–5113. [[CrossRef](#)]
53. Nikolaidis, R. Observation of Geodetic and Seismic Deformation with the Global Positioning System. Ph.D. Thesis, University of California, San Diego, CA, USA, 2002.
54. Xue, L.; Fu, Y.; Martens, H.R. Seasonal hydrological loading in the Great Lakes region detected by GNSS: A comparison with hydrological models. *Geophys. J. Int.* **2021**, *226*, 1174–1186. [[CrossRef](#)]
55. Grinsted, A.; Moore, J.C.; Jevrejeva, S. Application of the cross wavelet transform and wavelet coherence to geophysical time series. *Nonlinear Proc. Geophys.* **2004**, *11*, 561–566. [[CrossRef](#)]
56. Bian, Y.; Yue, J.; Li, Z.; Cong, K.; Li, W.; Xing, Y. Comparisons of GRACE and GLDAS derived hydrological loading and the impacts on the GPS time series in Europe. *Acta Geodyn. Geomater.* **2020**, *17*, 297–310. [[CrossRef](#)]
57. Van Dam, T.; Wahr, J.M.; Lavallee, D. A comparison of annual vertical crustal displacements from GPS and Gravity Recovery and Climate Experiment (GRACE) over Europe. *J. Geophys. Res.* **2007**, *112*, B03404. [[CrossRef](#)]
58. Scanlon, B.R.; Zhang, Z.; Save, H.; Sun, A.Y.; Schmied, H.M.; van Beek, L.P.H.; Wiese, D.N.; Wada, Y.; Long, D.; Reedy, R.C.; et al. Global models underestimate large decadal declining and rising water storage trends relative to GRACE satellite data. *Proc. Natl. Acad. Sci. USA* **2018**, *115*, E1080–E1089. [[CrossRef](#)] [[PubMed](#)]
59. He, M.; Shen, W.; Pan, Y.; Chen, R.; Ding, H.; Guo, G. Temporal-spatial surface seasonal mass changes and vertical crustal deformation in South China Block from GPS and GRACE measurements. *Sensors* **2017**, *18*, 99. [[CrossRef](#)]

- 
60. Zhang, L.; Tang, H.; Sun, W. Comparison of GRACE and GNSS seasonal load displacements considering regional averages and discrete points. *J. Geophys. Res. Solid Earth* **2021**, *126*, e2021JB021775. [[CrossRef](#)]
  61. Hao, M.; Freymueller, J.T.; Wang, Q.; Cui, D.; Qin, S. Vertical crustal movement around the southeastern Tibetan Plateau constrained by GPS and GRACE data. *Earth Planet. Sc. Lett.* **2016**, *437*, 1–8. [[CrossRef](#)]